

Entrainment of low Mach number thermals in stratified domains

EVAN H. ANDERS,^{1,2} DANIEL LECOANET,^{3,4} AND BENJAMIN P. BROWN^{1,2}

¹*Dept. Astrophysical & Planetary Sciences, University of Colorado – Boulder, Boulder, CO 80309, USA*

²*Laboratory for Atmospheric and Space Physics, Boulder, CO 80303, USA*

³*Princeton Center for Theoretical Science, Princeton, NJ 08544, USA*

⁴*Department of Astrophysical Sciences, Princeton, NJ 08544, USA*

(Received May 30, 2019; Revised ??; Accepted ??)

Submitted to ApJ

ABSTRACT

Large-scale convective flows called giant cells were once thought to transport the Sun’s luminosity in the solar convection zone, but recent observations have called their existence into question. In place of large-scale flows, some authors have suggested the solar luminosity may instead be transported by small droplets of rapidly falling, low entropy fluid. This “entropy rain” would propagate as dense vortex rings, analogous to rising buoyant thermals in the Earth’s atmosphere. In this work, we develop an analytical theory describing the evolution of dense, negatively buoyant thermals. We verify the theory with 2D and 3D simulations of laminar, axisymmetric thermals in highly stratified atmospheres. Our results suggest that entropy rain driven at the surface of the Sun could fall into two categories: a *stalling* regime in which the droplets slow down and expand, and a *falling* regime in which the droplets accelerate and shrink as they propagate downwards. We briefly discuss difficulties for the entropy rain hypothesis in both of these regimes. [This last sentence could be clarified, but I don’t know what we’re trying to say here](#)

Keywords: hydrodynamics — turbulence — entrainment

1. INTRODUCTION

Recent observations of solar convection have revealed a convective conundrum. Power spectra of horizontal velocities show weaker flows than anticipated at large length scales (Hanasoge et al. 2012; Greer et al. 2015). These observations cast doubt on the existence of giant cells driven by deep convection which should manifest as powerful, large-scale motions at the solar surface. This discrepancy between theory and observations has called into question our fundamental understanding of convection, sparking numerous targeted investigations into the nature of solar convection (Featherstone & Hindman 2016; O’Mara et al. 2016; Cossette & Rast 2016; Käpylä et al. 2017; Hotta 2017).

Rather than appealing to giant cells, Spruit (1997) hypothesized that convective motions in the Sun may be

primarily driven by cooling in narrow downflow lanes at the solar surface. Brandenburg (2016) incorporated this “entropy rain” concept into a non-local mixing length theory, and suggested the entropy rain could take the form of propagating vortex rings. However, Brandenburg (2016) does not include a fundamental aspect of entropy rain: it has lower entropy than the background atmosphere. Entropy rain is dense, and buoyancy forces will modify its dynamics.

It is important to understand how the filling factor of these basic convective elements is affected by their negative buoyancy. In the context of Earth’s atmosphere, “thermals,” or buoyant fluid regions which evolve into rising vortex rings, are thought to be basic unit of convection (e.g., Romps & Charn 2015). Atmospheric thermals are buoyant and rise, but the term is also used for dense, falling fluid. We thus study the entropy rain hypothesis by investigating the evolution of individual dense thermals.

Thermals in the Boussinesq limit have been well studied in the laboratory for decades (see e.g. Morton et al.

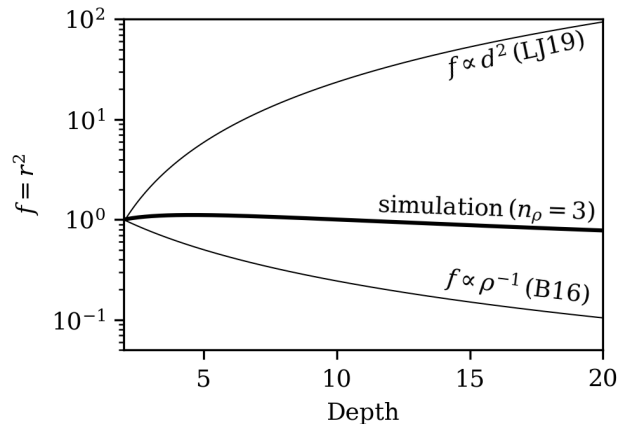


Figure 1. The filling factor of a dense thermal as a function of depth in an atmosphere which spans three density scale heights (the $n_\rho = 3$ case examined later in this work). Thin solid lines are the predictions for filling factor growth for the Boussinesq case (LJ19) and for pure horizontal compression (Brandenburg 2016).

1956; Scorer 1957), and more recently through Direct Numerical Simulation (DNS) (Lecoanet & Jeevanjee 2018). These studies find that thermals expand radially and decelerate as they propagate. Such an expansion may prevent entropy rain from reaching the bottom of the solar convection. However, this work does not include the effects of density stratification.

Ignoring entropy variations, Brandenburg (2016) suggests the filling fraction f of entropy rain should decrease like $f \propto \rho^{-1}$ for horizontal compression and $f \propto \rho^{-2/3}$ for spherical compression. On the other hand, the filling factor of Boussinesq thermals *increases* like $f \propto d^2$, where d is the depth of the thermal. These regimes are shown in Fig. 1, and compared to the true propagation of a numerically simulated dense thermal including both entropy variations and density stratification.

In this paper, we extend Lecoanet & Jeevanjee (2018) (hereafter LJ19) to study the propagation of low-Mach number, low-entropy thermals in stratified domains. We are specifically interested in how the buoyancy force affects the scaling of the thermal radius, or filling factor, with depth. If buoyancy dominant, it is possible that entropy rain would simply grow too large and stall before reaching the bottom of the solar convection zone. On the other hand, if the compression effects of Brandenburg (2016) are dominant, then these thermals could propagate to the bottom of the solar convection zone, validating the entropy rain picture.

In section 2, we develop a theoretical description of thermals in a stratified domain. In section 3, we describe the numerical experiments conducted in this work. In section 4, we compare our theory and simulation results.

Finally, in section 5, we discuss what our results imply for the entropy rain hypothesis.

2. THEORY

2.1. Phenomenological description of thermal evolution

Fig. 2 depicts the descent of 3D cold thermals released from rest in domains which span a different number of density scale heights (n_ρ). The left panel shows a weakly stratified domain with $n_\rho = 0.5$, whereas the right panel shows a strongly stratified domain with $n_\rho = 3$. In both cases, the thermal is initialized with a spherical negative entropy perturbation, which a diameter of 5% of the domain depth. This dense sphere spins up into an axisymmetric vortex ring, and the vertical cross section through this vortex ring shows two circular vorticity and entropy extrema. In the $n_\rho = 0.5$ simulation, the thermal grows with depth, similar to thermals in the Boussinesq regime. On the other hand, in the $n_\rho = 3$ simulation, the thermal’s radius remains approximately constant.

The goal of this paper is to understand the evolution of the thermal in the vortex ring stage. All of the thermals studied in this work are laminar, similar to the Hill vortices studied by Brandenburg (2016). Crucially, LJ19 showed little difference between the evolution of laminar and turbulent thermals in the Boussinesq limit. As a result, we leave studies of turbulent thermals in stratified domains for future work.

In the following sections, we will use the impulse of dense vortex rings derive their depth and radii with time.

2.2. Impulse

The evolution of thermals in the Boussinesq limit has been understood for decades (see e.g., LJ19 for a description and references). While many theoretical descriptions rely on self-similarity arguments, we will show how the impulse of a thermal controls its evolution.

The hydrodynamic impulse is defined as (Shivamoggi 2010),

$$\mathbf{I} = \frac{1}{2} \int_{\mathcal{V}} \mathbf{x} \times (\nabla \times (\rho \mathbf{u})) dV, \quad (1)$$

where \mathbf{x} is the position vector. The impulse is the time-integrated work which has acted on the fluid to result in the current fluid motion. It is thus unaffected by internal forces (e.g., pressure or viscous). Upon integration by parts, it is obvious that the impulse encompasses the momentum of the fluid within the volume \mathcal{V} . However, one can also show that the surface terms correspond to the momentum outside the volume \mathcal{V} (e.g. Akhmetov 2009). A thermal with volume \mathcal{V} , density ρ , and translating with velocity $w_{\text{th}} \hat{z}$ thus has an impulse [note that](#)

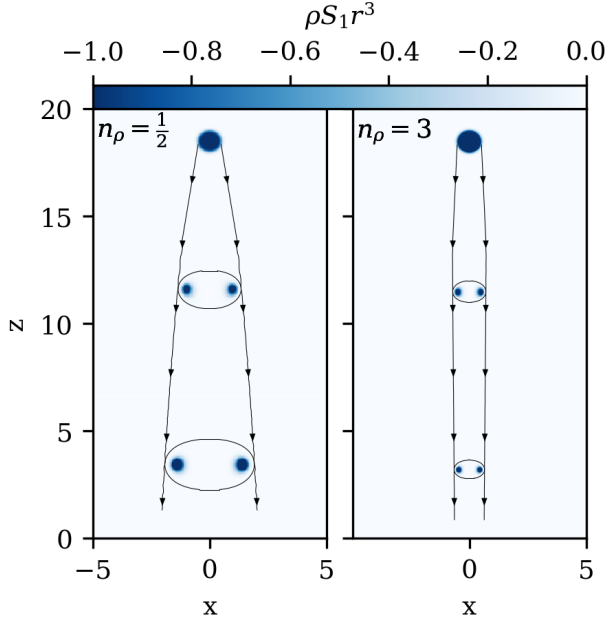


Figure 2. The mass-weighted entropy perturbation, $\rho S_1 r^3$, for two thermals. (left) a thermal in a weakly stratified domain with $n_\rho = 1/2$ density scale heights; (right) a thermal in a strongly stratified domain with $n_\rho = 3$. While both start with precisely the same initial condition, the thermal in low stratification expands with depth, whereas the thermal in strong stratification compresses with depth.

1+beta is the inverse of your old beta

$$I_z = (1 + \beta) \rho \mathcal{V} w_{\text{th}}, \quad (2)$$

where β is due to the “virtual mass effect” from the environmental fluid moving together with the thermal (Tarshish et al. 2018).

We now restrict our study to an ideal gas in the low Mach-number regime, in an adiabatic background. Due to rapid pressure equilibration in for low Mach-number flows, we can approximate Don't know if this is actually a good idea...

$$\frac{\rho_1}{\rho_0} \approx \frac{S_1}{c_P},$$

where S_1 is the specific entropy perturbation and c_P is the specific heat at constant pressure; thermodynamic variables are decomposed into background (subscript 0) and fluctuating (subscript 1) components.

The rate of change of change of the impulse is

$$\frac{d\mathbf{I}}{dt} = \int_{\mathcal{V}} \rho_1 \mathbf{g} dV,$$

because the surface terms completely cancel. It is useful to define the buoyancy perturbation,

$$B \equiv \int_{\mathcal{V}} \rho S_1 \frac{g}{c_P} dV. \quad (3)$$

such that

$$\frac{dI_z}{dt} = B. \quad (4)$$

In the limit of a low Mach-number, thin-core vortex ring, the impulse can be approximated as

$$I_z \approx \pi \rho r^2 \Gamma, \quad (5)$$

where r is the radius of the thermal from its axis of symmetry to its vorticity maximum, and $\Gamma = \int_{\mathcal{A}} (\nabla \times \mathbf{u}) dA$ is the circulation in a cross-section of the vortex ring. The circulation can change due to baroclinic torques,

$$\frac{d\Gamma}{dt} = \oint_{\mathcal{C}} g \frac{S_1}{c_P} \hat{\mathbf{z}} \cdot d\mathbf{x}, \quad (6)$$

where $\mathcal{C} = \partial\mathcal{A}$ is the contour around the thermal's vorticity. For the case of a vortex core in which the entropy perturbation is contained tightly in the core, as in Fig. 2, a contour can be drawn for which $S_1 \approx 0$. Thus, there are no net baroclinic torques, and we will treat the circulation of a developed vortex ring as a conserved quantity.

2.3. Model of thermal evolution

After spinning up, we assume that the thermal has a negative buoyancy, B_{th} , and circulation, Γ_{th} . While these thermals began as initial spherical perturbations, they act like vortex rings which evolved from a “virtual origin” where the vortex ring had zero radius. From this virtual origin, the vortex ring's impulse would have been I_0 at time $t = 0$ when the true thermal is released from rest.

We find the thermal undergoes weak detrainment, so the negative buoyancy of the thermal decreases slightly in time (Fig. 3b). We thus express the buoyancy perturbation as

$$B \approx \chi B_{\text{th}}, \quad (7)$$

where χ is a constant of $\mathcal{O}(1)$ which represents this detrainment. We then integrate Eqn. 4,

$$I_z = \chi B_{\text{th}} t + I_0.$$

Combining this with Eqn. 5, we retrieve our first main result,

$$r = \sqrt{\frac{\chi B_{\text{th}} t + I_0}{\pi \rho \Gamma_{\text{th}}}}. \quad (8)$$

Recall there are no net baroclinic torques, so stays Γ_{th} nearly constant (Fig. 3a). In the Boussinesq limit where $\rho \rightarrow \text{constant}$, we retrieve the $r \propto \sqrt{t}$ scaling found in LJ19. In the limit of strong stratification, $r \propto \rho^{-1/2}$, corresponding to purely horizontal compression, with $r^2 \propto \rho^{-1}$ (Brandenburg 2016).

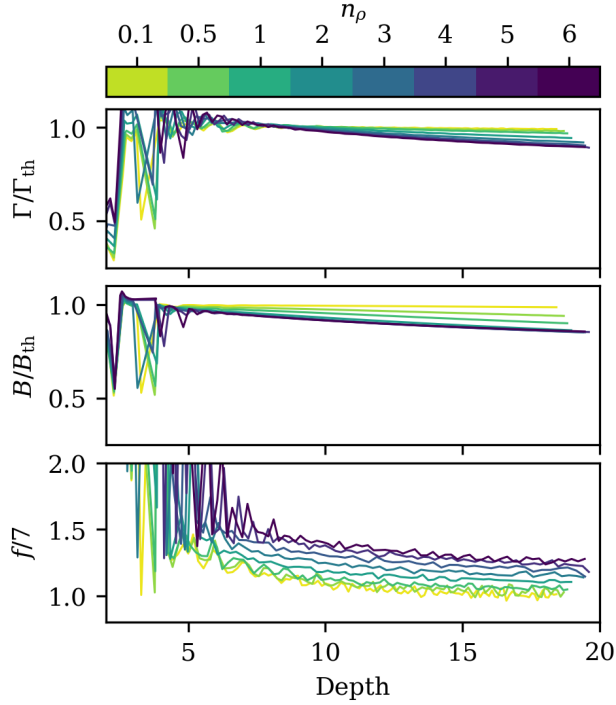


Figure 3. Evolution of circulation, buoyancy perturbation, and volume factor in thermal simulations. All are nearly constant after an initial spin-up phase. With increasing stratification, we see marginally more detrainment (middle panel). The volume factor can be approximated to be $\mathcal{O}(7)$ for all of our simulations.

To solve for the vertical evolution of the thermal, we can use equation 2. We approximate the volume as $\mathcal{V} = fr^3$, where f is a parameter which we take to be constant. We find [fix this equation](#)

$$\rho^{-1/2}w_{\text{th}} = \left(\frac{(\pi\Gamma_{\text{th}})^{3/2}}{f} \right) \frac{\beta\chi B_{\text{th}}t + I_0}{(\chi B_{\text{th}}t + I_0)^{3/2}}. \quad (9)$$

Defining the thermal velocity $w_{\text{th}} \equiv dz_{\text{th}}/dt$, and assuming I_0 is small, we have [fix this equation](#)

$$\frac{dz_{\text{th}}}{\rho(z_{\text{th}})^{1/2}} = \left(\frac{\beta(\pi\Gamma_{\text{th}})^{3/2}}{f(\chi B_{\text{th}})^{1/2}} \right) \frac{dt}{t^{1/2}}. \quad (10)$$

This can be easily integrated given an atmospheric stratification $\rho(z)$.

To summarize, we model thermals as thin-core vortex rings. The vortex ring is parameterized by its buoyancy perturbation and circulation, which are assumed to be nearly constant after spin-up. The impulse increases in magnitude due to buoyancy forces (Eqn. 4), and allows us to relate the size of the vortex ring (Eqn. 5) to the momentum of the thermal and its ambient fluid (Eqn. 2). Assuming the thermals' volume is spheroidal and that the virtual mass effect and detrainment can be parameterized as constants, we arrive at Eqn. 10.

2.4. Solution polytrope atmospheres

In this work, we study an ideal gas with an adiabatic index of $\gamma = 5/3$. An adiabatic polytrope satisfies

$$T_0 = 1 + (\nabla_{\text{ad}})(z - L_z), \quad (11)$$

$$\rho_0 = T_0^{m_{\text{ad}}}, \quad (12)$$

where $m_{\text{ad}} = (\gamma - 1)^{-1}$. All thermodynamic quantities are nondimensionalized such that $\rho_0 = T_0 = 1$ at $z = L_z$.

Integrating Eqn. 10 under this polytropic density stratification, we find

$$z_{\text{th}} = \nabla_{\text{ad}}^{-1} \left[\left(\frac{2C}{\alpha} \sqrt{t + t_{\text{off}}} + T_{\text{th},0}^{1/\alpha} \right)^\alpha - 1 \right] + L_z, \quad (13)$$

where $C \equiv \beta\pi^{3/2}\nabla_{\text{ad}}/f\sqrt{\Gamma_{\text{th}}^3/(\chi B_{\text{th}})}$ and the temperature at the virtual origin is $T_{\text{th},0} = 1 + \nabla_{\text{ad}}(z_{\text{th},0} - L_z)$. The thermal is at the virtual origin, $z = z_0$, at time $t = -t_{\text{off}}$. The constant $\alpha^{-1} = 1 - m_{\text{ad}}/2$, and in the limit of large stratification, we find that $z_{\text{th}} \propto t^2$ for our case of $\alpha = 4$.

In our simulations, the thermal is initialized as a uniform sphere of dense fluid but it quickly spins up into a vortex ring. While we do not attempt to model the spin-up phase in this paper, it can be parameterized by the buoyancy B_{th} , circulation Γ_{th} , as well as the virtual origin $z_{\text{th},0}$, and temporal offset t_{off} . Our theory also involves the volumetric aspect ratio of the thermal f , the detrainment fraction χ , and the effective buoyancy β . These appear to be constant or only weakly dependent on the stratification for the thermals we have simulated.

3. NUMERICAL EXPERIMENT

As a result of our theory being largely derived in the anelastic, axisymmetric limit, we have chosen to focus the bulk of our attention on our 2D, axisymmetric anelastic simulations. We choose to focus on 2D simulations, as they allow us to more easily study high density stratifications using highly reproducible simulations whose computational expense is low. We verify that select anelastic simulations produce the same results as 3D fully compressible simulations in cartesian domains.

While natural processes are very turbulent, we have chosen to study the evolution of laminar thermals here. As we are not aware of a developed laminar theory in the stratified regime in the literature, like the one developed here, it is useful to restrict our study to the laminar case to determine the validity of our theory. Furthermore, [LJ19](#) showed in the Boussinesq limit that the measured entrainment of turbulent thermal vortex rings is well described by laminar theory, and we have no reason to believe that result should not hold for the stratified case.

As a result, we leave studies of turbulent thermals to future work.

3.1. Anelastic Simulations

The LBR anelastic equations are (Lecoanet et al. 2014),

$$\nabla \cdot \mathbf{u} = -w \partial_z \ln \rho_0, \quad (14)$$

$$\begin{aligned} \partial_t \mathbf{u} + \mathbf{u} \cdot \nabla \mathbf{u} = \\ -\nabla \varpi + S_1 \hat{z} + \frac{1}{\rho_0 \text{Re}} \left[\nabla^2 \mathbf{u} + \frac{1}{3} \nabla (\nabla \cdot \mathbf{u}) \right] \end{aligned} \quad (15)$$

$$\begin{aligned} \partial_t S_1 + \mathbf{u} \cdot \nabla S_1 = \\ \frac{1}{\text{Re}} \left(\frac{1}{\text{Pr} \rho_0 c_P} [\nabla^2 S_1 + \partial_z \ln T_0 \cdot \partial_z S_1] \right. \\ \left. + \frac{-(\nabla_{\text{ad}})}{\rho_0 T_0} \sigma_{ij} \partial_{x_i} u_j \right), \end{aligned} \quad (16)$$

where $\bar{\sigma}$ is the viscous stress tensor in units of inverse time. In our azimuthally symmetric, cylindrical domain, we assume that $\partial_\phi = 0$; as the initial conditions of our simulations are at rest and have no azimuthal velocity, u_ϕ , we explicitly impose that $u_\phi = 0$; therefore $\mathbf{u} = u_r \hat{r} + w \hat{z}$.

These equations have been nondimensionalized in the same manner as in LJ19 such that the length scale is the diameter of the initial thermal perturbation and the velocity scale is the freefall velocity. The timescale is thus the freefall crossing time of this unit length. These equations are then fully specified in terms of the Reynolds number and Prandtl number,

$$\text{Re} = \frac{u_{\text{th}} L_{\text{th}}}{\nu}, \quad \text{Pr} = \frac{u_{\text{th}} L_{\text{th}}}{\chi}, \quad u_{\text{th}}^2 = \frac{g L_{\text{th}} \Delta s}{c_P}, \quad (17)$$

where u_{th} is the freefall velocity, L_{th} is the thermal length scale, and Δs is the magnitude of the specific entropy signature of the thermal.

We choose an atmospheric model in which the dynamic viscosity, $\mu = \rho_0 \nu$, and the thermal conductivity, $\kappa = \rho_0 \chi$, are both uniform and constant in time. We make this choice as the mass-weighted diffusivities, μ and κ , appear in the density-weighted momentum and entropy equations, and we find the density-weighted entropy and momentum to be key quantities in our thermal theory. The diffusivities ν and χ therefore scale inversely with the density. As the diffusivities scale with depth, Re is specified at the thermal's initial depth. All simulations conducted in this work use a value of $\text{Re} = 600$ and $\text{Pr} = 1$.

3.2. Fully Compressible Simulations

In order to verify the validity of our 2D Anelastic simulations, we evolve select thermals according to the 3D

Navier Stokes equations in a cartesian domain. We use the $(T, \ln \rho)$ formulation of the equations in which we have previously studied fully compressible convection at low and high Mach number (Lecoanet et al. 2014; Anders & Brown 2017),

$$\frac{\partial \ln \rho_1}{\partial t} + \epsilon^{-1} (\mathbf{u} \cdot \nabla \ln \rho_0 + \nabla \cdot \mathbf{u}) = -\mathbf{u} \cdot \nabla \ln \rho_1, \quad (18)$$

$$\begin{aligned} \frac{\partial \mathbf{u}}{\partial t} + \nabla T_1 + T_1 \nabla \ln \rho_0 + T_0 \nabla \ln \rho_1 = \\ -\epsilon T_1 \nabla \ln \rho_1 + \frac{1}{\rho \text{Re}} \left[\nabla^2 \mathbf{u} + \frac{1}{3} \nabla (\nabla \cdot \mathbf{u}) \right] \\ \frac{\partial T_1}{\partial t} + \epsilon^{-1} [\mathbf{u} \cdot \nabla T_0 + (\gamma - 1) T_0 \nabla \cdot \mathbf{u}] = \\ -[\mathbf{u} \cdot \nabla T_1 + (\gamma - 1) T_1 \nabla \cdot \mathbf{u}] + \frac{1}{\rho c_V \text{Re}} \left[\frac{1}{\text{Pr}} \nabla^2 T_1 + \sigma_{ij} \partial_{x_i} u_j \right]. \end{aligned} \quad (19)$$

These equations have been nondimensionalized on the same length and time scales as the anelastic equations, use the same atmospheric profiles and assumptions, and we have explicitly assumed that the background atmosphere $(T_0, \ln \rho_0)$ is in hydrostatic and thermal equilibrium in the writing of these equations. The new parameter $\epsilon = u_{\text{th}}^2$ is the magnitude of entropy perturbations and sets the Mach number of the thermal flows, and we use $\epsilon = 10^{-4}$ in this work.

In setting the specific entropy to an equivalent condition to that specified in Eqn. 22, we note that it is essential that the initial perturbation be in pressure equilibrium. The set of initial conditions that achieves this is

$$\ln \rho_1 = S_1 / c_P, \quad T_1 = T_0 (e^{-\epsilon \ln \rho_1} - 1) / \epsilon. \quad (21)$$

3.3. Initial conditions

To initialize the simulation, we specify a spherical initial specific entropy perturbation,

$$S_1 = \frac{1}{2} \left[\text{erf} \left(\frac{r' - r_{\text{th}}}{\delta} \right) - 1 \right]. \quad (22)$$

Here, $r' = \sqrt{r^2 + (z - z_0)^2}$, where $z_0 = L_z - 3r_{\text{th}}$, with the thermal radius set as $r_{\text{th}} = 0.5$, and a smoothing width, $\delta = 0.1$. As mentioned previously, $\text{Re} = 600$ and $\text{Pr} = 1$ are specified at the thermal's initial depth, $z = z_0$.

3.4. Numerics

We evolve our simulations forward in time using the Dedalus¹ pseudospectral framework (Burns et al. 2016,

¹ <http://dedalus-project.org/>

2019). For our 2D simulations, we use using an implicit-explicit (IMEX), third-order, four-stage Runge-Kutta timestepping scheme RK443 (Ascher et al. 1997), and for our 3D simulations we use the second-order semi-implicit backward differentiation formulation SBDF2 (Wang & Ruuth 2008).

Our 3D simulations are decomposed on Fourier bases in the horizontal directions ($x, y \in [-L_r, L_r]$) and Chebyshev bases vertically ($z \in [0, L_z]$) with impenetrable, stress free, fixed-temperature boundary conditions at the upper and lower boundaries ($T_1 = w = \partial_z u = \partial_z v = 0$ at $z = [0, L_z]$). Our 2D simulations are decomposed on a Fourier ($z \in [0, L_z]$) and Chebyshev ($r \in [0, L_r]$) domain, with boundary conditions of $\partial_r S_1 = w = (\nabla \times \mathbf{u})_\phi = 0$ at $r = L_r$ and $u = \partial_r(w) = \partial_r(S_1) = 0$ at $r = 0$.

All of the code used to perform the simulations in this work can be found online in the supplementary materials in a Zenodo repository (CREATE AND CITE REPO).

4. RESULTS

In Fig. 4a, we show the measured depth $d_{th} = L_z - z_{th}$ of the thermal as a function of time for low and high stratification. At very low stratification (e.g., $n_\rho = 0.1$), the thermal is small compared to the local density scale height at all depths, and it evolves roughly according to the Boussinesq prediction of $d \propto \sqrt{t}$. As the stratification increases, the thermal begins to transit the domain more quickly and approaches the limit of $d \propto t^2$ predicted in the highly stratified limit of Eqn. 13. The theoretical fits for depth from the prediction of Eqn. 13 are plotted over the measured data. Unsurprisingly, the theoretical fits are poor for early times when the thermal is spinning up from its initial spherical state into the vortex ring state. Once the thermal is spun up into a vortex ring, the theory shows remarkable agreement with the measured data.

In Fig. 4b, we show the corresponding thermal velocity as a function of depth with the theory overplotted again. As anticipated, low density ($n_\rho = 0.1$) thermals decelerate with depth. We find that with increasing stratification, this deceleration stops and sufficiently stratified runs ($n_\rho \geq 3$) experience acceleration of the thermal.

In Fig. 5a, we display measured thermal radius vs. depth, with a point-by-point comparison of our 2D Anelastic and 3D Fully Compressible cases. In the low stratification limit, the radius of the thermal grows linearly with depth, $r \propto d$, aligning with the Boussinesq limit shown in LJ19. This growth of the thermal is the result of entrainment of environmental fluid and accompanies deceleration like $w \propto d^{-1}$ in the Boussinesq

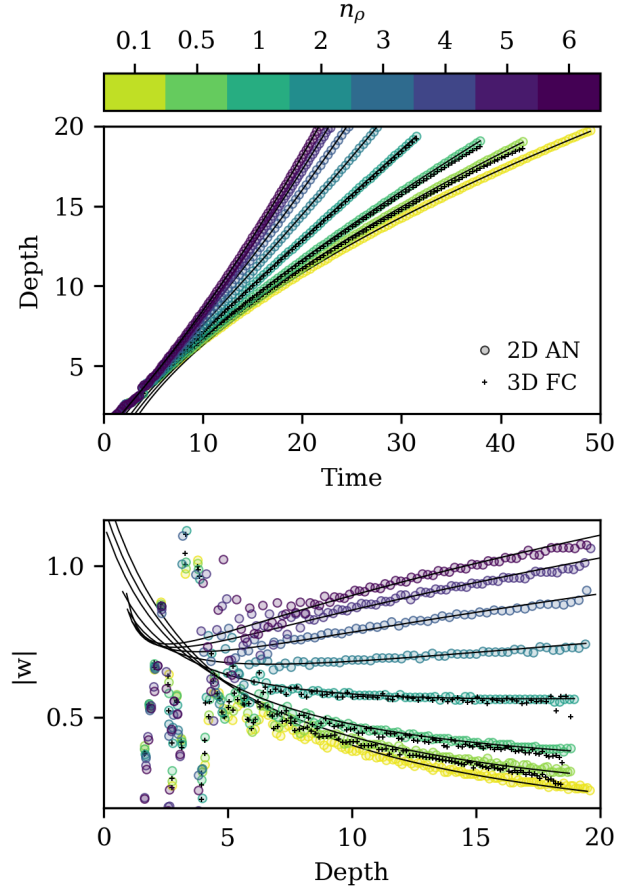


Figure 4. The measured depths of thermals as a function of time for all 2D Anelastic and 3D Fully compressible simulations conducted in this work are shown in (a). The corresponding thermal velocities as a function of depth are shown in (b). Overplotted in a thin solid line for each case are our theoretical predictions from section 2 given the parameters in table 1.

limit, as is shown in Fig. 4b. However, as stratification increases, the thermal entrainment of environmental fluid decreases and it experiences less expansion. In the limit of large stratification ($n_\rho \geq 3$), thermals begin contracting with depth. This lessened entrainment is, unsurprisingly, accompanied by greater acceleration of the thermal (Fig. 4).

In Fig. 5b, the fractional difference in radius vs. depth between 3D fully compressible and 2D anelastic cases is shown for the $n_\rho = [0.5, 1, 2]$ cases studied here. Aside from early in the simulation, when the thermal is spinning up, and late in the simulation, when the 3D simulations begin interacting with the impenetrable boundary at the bottom of the domain, the 2D anelastic and 3D fully compressible simulations agree well. We find differences in the radius of less than 1% throughout the bulk of the thermal evolution for the cases studied here. This

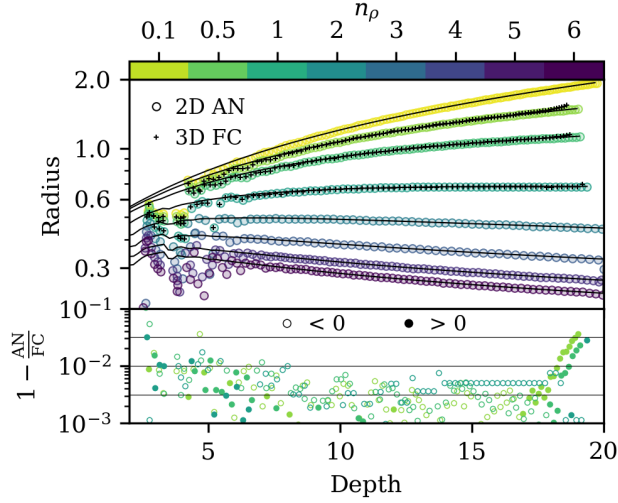


Figure 5. Measured values of radius vs. depth are plotted for both the 2D anelastic and 3D fully compressible simulations in (a). For completeness, we also include the cases in which we only studied the 2D anelastic simulations. For the cases in which only the anelastic equations were solved, the theory is overplotted in a thin solid line, and similar agreement between simulations and theory is found for the cases where both equations sets were used. The fractional difference between anelastic and fully compressible results are shown in (b).

gives us confidence that our high stratification anelastic simulations are producing reliable results. Furthermore, this close agreement between low Mach number Fully Compressible simulations and Anelastic simulations parallels the agreement between the equation sets seen in Lecoanet et al. (2014).

The measured values of each of the parameters described in section 2 for each of our simulations are presented in table 1. As anticipated, β is $\mathcal{O}(0.5)$ and χ is $\mathcal{O}(1)$, with both decreasing slightly in value with increasing stratification, which is perhaps unsurprising in light of Fig. 3. In all cases, the buoyancy B_{th} is similar to the integrated buoyancy in the initial conditions, with some losses due to detrainment in the spin-up. In our nondimensional units, we also find that the circulation is $\mathcal{O}(-2)$ for each of our cases, and decreases with increasing stratification (and decreasing vortex size).

Throughout this section, the thermal’s depth and radius refer respectively to the atmospheric depth and the radius from the axis of symmetry at which the vortex ring’s entropy minimum is located. The velocity is simply the derivative with respect to time of that measured depth. For specifics on how these measurements are conducted in our simulations, we refer the reader to appendix A.

5. CONCLUSION & DISCUSSION

In this paper we developed a simple theory of the evolution of negatively buoyant vortex rings in stratified atmospheres. We showed that this theory predicts that dense thermals will experience less entrainment than boussinesq thermals due to increasing atmospheric density with depth. We performed 2D anelastic simulations of thermal evolution for varying degrees of stratification and showed that our parameterized theory describes the evolution of thermals in these systems remarkably well. Furthermore, we verified the validity of our anelastic simulations with select 3D fully compressible simulations of thermal evolution and found agreement to under 1%.

We note that the evolution of dense thermals in stratified domains is complex, and neither the assumption of horizontal compression (as in e.g., Brandenburg 2016) or the evolution of thermals in the Boussinesq regime (as in LJ19) fully describes the behavior of these events fully. Rather, results fall somewhere in between, and theory and simulations suggest that there are two regimes of downflowing thermal behavior:

1. A low-stratification “stalling” regime, in which the thermal entrains environmental fluid and slows down, acting much like the Boussinesq regime, and
2. A high-stratification “falling” regime, in which the thermal falls fast enough that compression due to the atmospheric stratification results in minimal entrainment and the thermal accelerates as it falls deeper into the atmosphere.

However, we note that both the falling and stalling regimes observed here could result in interesting problems for the entropy rain hypothesis. If solar convection were comprised of thermals in the stalling regime, it is unlikely that such elements would ever make it to the base of the solar convection zone. Rather, we expect that they would stall closer to the solar surface and deposit their entropy signature there. This could be seen as agreeing with the hypothesis of supergranulation as the largest buoyantly driven scale of solar motion.

On the other hand, if solar convection is comprised of thermals in the falling regime, then it is not out of the question for solar surface elements to reach deep into the Sun. While vortex rings in the falling regime would theoretically be able to reach the bottom of the solar convection zone, the compression effects that occur as they shrink could cause problems. For example, it is possible that these thermals could shrink to the point where conductivity becomes important, or as their length scales decrease and velocities increase, vis-

Table 1. Simulation output parameterization

n_ρ	$z_{\text{th},0}$	t_{off}	B_{th}	Γ_{th}	f	χ	β
2D Anelastic Simulations							
0.1	24.4	0.166	-0.547	-2.17	7.01	1.04	0.499
0.5	24.1	0.704	-0.568	-2.12	7.04	0.976	0.490
1	23.7	1.09	-0.601	-2.05	7.07	0.915	0.480
2	22.3	1.26	-0.712	-1.89	7.08	0.841	0.456
3	21.2	1.01	-0.946	-1.73	7.08	0.808	0.436
4	20.5	0.622	-1.47	-1.59	7.10	0.793	0.422
5	20	0.327	-2.70	-1.49	7.15	0.786	0.414
6	19.8	0.064	-5.73	-1.43	7.16	0.787	0.408
3D Fully Compressible Simulations							
0.5	23.8	0.583	-0.568	-2.12	6.66	0.978	0.452
1	23.5	1.26	-0.601	-2.05	6.88	0.902	0.454
2	22.4	1.53	-0.711	-1.89	7.08	0.822	0.450

NOTE—

cous heating could become an important effect and essentially erase the buoyant signature of these entropy rain droplets.

In Fig. ??, we extrapolate the results of our simulations to solar convection. For each simulation performed, we show the behavior of our thermals if they were to fall the first $n_\rho = 10$ density scale heights of the solar convection zone, rather than the few that we were able to simulate here. We see blahblahblah.

This work was supported by NASA Headquarters under the NASA Earth and Space Science Fellowship Program – Grant 80NSSC18K1199. This work was additionally supported by NASA LWS grant number NNX16AC92G. Computations were conducted with support by the NASA High End Computing (HEC) Program through the NASA Advanced Supercomputing (NAS) Division at Ames Research Center on Pleiades with allocation GID s1647.

APPENDIX

A. THERMAL MEASUREMENTS

Throughout this work, we frequently report the thermal’s radius or its depth. We measure the thermal’s radius and height as the radius from the axis of symmetry and the height from the bottom of the domain at which the thermal’s vortex core is located. To measure this, we locate the maxima of the entropy. To find the entropy maxima vertically, we integrate $\int \rho S_1 r dr$ in our Dedalus domain, then use the spectral data of that profile to sample it on a 4096 point grid vertically, and we take the location of the minima on that grid to be the thermal height. To find the entropy maxima horizontally, we integrate $\int \rho S_1 dz$ in our Dedalus domain, then sample the spectral data onto a 2048-point radial grid, and take the minima of that profile to be the radius of the thermal. In order to find the thermal’s velocity as a function of time, we use a five-point stencil to differentiate the thermal’s depth, d ,

$$w_{\text{th}}(t) = \frac{d}{dt} d_{\text{th}}(t) = \frac{-d_{\text{th}}(t + 2\Delta t) + 8d_{\text{th}}(t + \Delta t) - 8d_{\text{th}}(t - \Delta t) + d_{\text{th}}(t - 2\Delta t)}{12\Delta t}$$

Integral quantities, such as the circulation, Γ , the buoyancy, B , and the volume, \mathcal{V} require us to first determine what fraction of the domain constitutes the thermal. To do so, we use the thermal tracking algorithm described in appendix B to determine the radial contour that outlines the thermal as a function of height, \mathcal{C} . We then use this contour to find our integral quantities,

$$\Gamma = \int_0^{\mathcal{C}} \int_0^{L_z} (\nabla \times \mathbf{u})_\phi dz dr, \quad B = 2\pi \int_0^{\mathcal{C}} \int_0^{L_z} \rho S_1 r dz dr, \quad \mathcal{V} = 2\pi \int_0^{\mathcal{C}} \int_0^{L_z} r dz dr. \quad (\text{A1})$$

B. THERMAL TRACKING

We use a thermal tracking algorithm very similar to the one used in [Lecoanet & Jeevanjee \(2018\)](#) and inspired by the work of [Romps & Charn \(2015\)](#) in order to determine the full extent of the thermal, as pictured by the elliptical

Table 2. Table of simulation information

n_ρ	L_r	nr or nx = ny	nz	$t_{\text{evolution}}$	safety
2D Anelastic Simulations					
0.1	5	128	512	50	0.6
0.5	5	128	512	45	0.6
1	5	128	512	41	0.6
2	5	256	1024	34	0.4
3	5	256	1024	29	0.4
4	5	256	1024	26	0.3
5	5	256	1536	25	0.14
6	5	256	1536	23	0.08
3D Fully Compressible Simulations					
0.5	5	256	512	42.5	0.2
1	4	256	512	38	0.2
2	3.5	256	1536	31.75	0.2

NOTE—

outlines in Fig. 2 We begin by measuring the thermal’s velocity versus time, w_{th} , as described in appendix A. We then calculate the streamfunction of the velocity field as in Romps & Charn (2015),

$$\frac{\partial \psi}{\partial r} = 2\pi \rho r (w - w_{\text{th}}), \quad (\text{B2})$$

with the boundary condition that $\psi = 0$ at $r = 0$. The contour defined by $\psi = 0$ from this solution is taken to be the contour bounding the thermal, \mathcal{C} .

C. TABLE OF SIMULATIONS

Information regarding the simulation resolution and CFL safety factor for each of the simulations presented in this work is contained in table 2. The Python scripts used to perform all simulations and analysis in this work are stored online in a Zenodo repository CITE.

REFERENCES

- Akhmetov, D. G. 2009, Vortex rings (Berlin, Heidelberg: Springer Berlin Heidelberg), 1–151, doi:10.1007/978-3-642-05016-9
- Anders, E. H., & Brown, B. P. 2017, Physical Review Fluids, 2, 083501
- Ascher, U. M., Ruuth, S. J., & Spiteri, R. J. 1997, Applied Numerical Mathematics, 25, 151
- Brandenburg, A. 2016, ApJ, 832, 6
- Burns, K., Vasil, G., Oishi, J., Lecoanet, D., & Brown, B. 2016, Dedalus: Flexible framework for spectrally solving differential equations, Astrophysics Source Code Library, , ascl:1603.015
- Burns, K. J., Vasil, G. M., Oishi, J. S., Lecoanet, D., & Brown, B. P. 2019, arXiv e-prints, arXiv:1905.10388
- Cossette, J.-F., & Rast, M. P. 2016, ApJ, 829, L17
- Featherstone, N. A., & Hindman, B. W. 2016, ApJ, 830, L15
- Greer, B. J., Hindman, B. W., Featherstone, N. A., & Toomre, J. 2015, ApJ, 803, L17
- Hanasoge, S. M., Duvall, T. L., & Sreenivasan, K. R. 2012, Proceedings of the National Academy of Science, 109, 11928
- Hotta, H. 2017, ApJ, 843, 52
- Käpylä, P. J., Rheinhardt, M., Brandenburg, A., et al. 2017, ApJ, 845, L23
- Lecoanet, D., Brown, B. P., Zweibel, E. G., et al. 2014, ApJ, 797, 94
- Lecoanet, D., & Jeevanjee, N. 2018, arXiv e-prints, arXiv:1804.09326
- Morton, B. R., Taylor, G., & Turner, J. S. 1956, Proceedings of the Royal Society of London Series A, 234, 1

- O'Mara, B., Miesch, M. S., Featherstone, N. A., & Augustson, K. C. 2016, *Advances in Space Research*, 58, 1475
- Romps, D. M., & Charn, A. B. 2015, *Journal of the Atmospheric Sciences*, 72, 2890
- Romps, D. M., & Charn, A. B. 2015, *Journal of Atmospheric Sciences*, 72, 2890
- Scorer, R. S. 1957, *Journal of Fluid Mechanics*, 2, 583
- Shivamoggi, B. K. 2010, *Physics Letters A*, 374, 4736
- Spruit, H. C. 1997, *Mem. Soc. Astron. Italiana*, 68, 397
- Tarshish, N., Jeevanjee, N., & Lecoanet, D. 2018, *Journal of Atmospheric Sciences*, 75, 3233
- Wang, D., & Ruuth, S. J. 2008, *Journal of Computational Mathematics*, 26, 838